Tuning the dual-active sites of ZIF-67 derived porous nanomaterials for boosting oxygen catalysis and rechargeable Zn-air batteries

Zeyi Zhang[1,§], Yangyang Tan[1,§], Tang Zeng[1], Liyue Yu[1], Runzhe Chen[1], Niancai Cheng[1] (✉), Shichun Mu[2] (✉), and Xueliang Sun[3] (✉)

[1] College of Materials Science and Engineering, Fuzhou University, Fuzhou 350108, China
[2] State Key Laboratory of Advanced Technology for Materials Synthesis and Processing, Wuhan University of Technology, Wuhan 430070, China
[3] Department of Mechanical and Materials Engineering, University of Western Ontario, London, ON N6A 5B9, Canada
[§] Zeyi Zhang and Yangyang Tan contributed equally to this work.

ABSTRACT

The rational control of the active site of metal-organic frameworks (MOFs) derived nanomaterials is essential to build efficient bifunctional oxygen reduction/evolution reaction (ORR/OER) catalysts. Accordingly, through designing and constructing a Co_3O_4-Co heterostructure embedded in Co, N co-doped carbon polyhedra derived (Co_3O_4-Co@NC) from the *in-situ* compositions of ZIF-67 and cobalt nanocrystals synthesized by the strategy of *in-situ* $NaBH_4$ reduction, the dual-active site (Co_3O_4-Co and Co-N_x) is synchronously realized in a MOFs derived nanomaterials. The formed Co_3O_4-Co@NC shows excellent bifunctional electrocatalytic activity with ultra-small potential gap ($\Delta E = E_{j=10}$ (OER) $- E_{1/2}$ (ORR)) of 0.72 V, which surpasses the commercial Pt/C and RuO_2 catalysts. The theory calculation results reveal that the excellent bifunctional electrocatalytic activity can be attributed to the charge redistribution of Co of Co-N_x induced by the synergistic effects of well-tuned active sites of Co_3O_4-Co nanoparticle and Co-N_x, thus optimizing the rate-determining step of the desorption of O_2* intermediate in ORR and OH* intermediate in OER. The rechargeable Zn-air batteries with our bifunctional catalysts exhibit superior performance as well as high cycling stability. This simple-effective optimization strategy offers prospects for tuning the active site of MOF derived bifunctional catalyst in electrochemical energy devices.

KEYWORDS

dual-active sites, bifunctional oxygen electrocatalysts, metal–organic frameworks, Zn-air batteries, density functional theory (DFT)

1   Introduction

Rechargeable zinc-air batteries (ZABs) has broad application prospects in the energy field owing to its high energy density (1,086 Wh·kg⁻¹), eco-friendliness, non-toxicity and sustainability [1–6]. Nevertheless, the commercialization of rechargeable ZABs is limited by their low energy conversion efficiency, originating from the slow oxygen reduction reaction/oxygen evolution (ORR/OER) kinetics and the corresponding increase in high overpotential [7–10]. At present, Pt and Ru/Ir oxides are the efficient ORR and OER catalysts, respectively, but, low storage capacity, high cost and unifunctional catalytic activity hamper their large-scale application in rechargeable ZABs [11–15]. Furthermore, bifunctional ORR/OER electrocatalysts have been prove to not only possess higher performance than two separate unifunctional catalysts in rechargeable ZABs, but also make renewable energy conversion and storage systems simpler [16]. Thus, the designing and/or developing cost-effective and highly performance non-precious-metal bifunctional ORR/OER catalysts is highly desirable.

Recently, metal-organic frameworks (MOFs) as precursors

have been intensively studied for developing high performance of bifunctional ORR/OER electrocatalysts [17–20]. For instance, the porous nanomaterials derived from zeolite imidazole framework-67 (ZIF-67) have indicated excellent bifunctional ORR/OER activities, resulting in high performance of rechargeable ZABs [21–23]. The high bifunctional ORR/OER activities originated from the synergistic effects of Co-based nanoparticle and Co-N_x active sites fabricated during the high pyrolysis of the ZIF-67 precursors. It is reported that the Co-N_x active site in the ZIF-67 derived porous nanomaterials has a superior ORR activity comparable to precious metal catalysts in alkaline solutions [24–27]. Simultaneously, the formation of cobalt oxides with the mixed-valence cobalt (II, III) possesses high OER catalytic activity in the alkaline environment [28–30]. However, the short distance of Co atoms in ZIF-67 frameworks makes Co atoms aggregate easily into nonuniform large particles during high-temperature pyrolysis procedure, resulting in the large loss of active sites and poor control of the catalyst morphology and then decreases the bifunctional catalytic activities. Therefore, it is very important for the ZIF-67 derived electrocatalysts to tune the active sites of

Co-N$_x$ and cobalt oxides to boost the bifunctional ORR/OER activities. In addition to the above concerns about the tuning cobalt-based active sites, it is also necessary to construct micro/nano structures to expose sufficient active sites and favor fast mass/charge transport behavior [31, 32]. Although the porous nanomaterials derived from ZIF-67 has a three-dimensional (3D) polyhedral structure, only limited amounts of surface Co based moieties are effective catalytic sites, while the internal active sites are difficult to be entirely utilized due to the narrow channels [33]. Therefore, reconstructing the micro/nano pore structure of ZIF-67 derived nanomatrials is attractive for exposing more active sites and improving the performance.

Herein, we designed a high performance of bifunctional ORR/OER electrocatalyst through tuning the dual-active sites (cobalt oxide and Co-N$_x$) and pore structure of a heterostructure Co$_3$O$_4$-Co NPs embedded in Co, N co-doped carbon polyhedra derived from the compositions of ZIF-67 and cobalt nanocrystals. The compositions of ZIF-67 and cobalt nanocrystals (Co@ZIF-67) were synthesized by the strategy of *in-situ* NaBH$_4$ reduction during assembly of Co^{2+} and 2-methylimidazole. The unique structure of cobalt nanocrystals generated by NaBH$_4$ in ZIF-67 not only creates more micropore structure in ZIF-67-derived nanomaterials, but also prevents Co atoms in coordination from further migration and agglomeration into large particles during high-temperature pyrolysis due to steric hindrance effect. More importantly, our strategy of *in-situ* NaBH$_4$ reduction tunes the active sites, especial OER active sites on the ZIF-67 derived nanomaterials. As a result, when integrating our optimized bifunctional ORR/OER electrocatalysts (Co$_3$O$_4$-Co@NC-2) into the air electrode of zinc air battery, high performance and service life with more than 200 h are achieved. Experimental results and theory calculations reveal that the excellent ORR/OER catalytic activities of Co$_3$O$_4$-Co@NC-2 originate from the synergistic effects of Co-based nanoparticle and Co-N$_x$ active sites, in which the charge redistribution of Co of Co-N$_x$ sites induced by electron coupling with the internal heterostructure Co$_3$O$_4$-Co nanoparticles thus optimizing the desorption of O$_2^*$ intermediate in ORR and OH* intermediate in OER.

2   Results and discussion

In order to tune the cobalt-based active sites and pore structure of ZIF-67 derived carbon nanomaterials, we firstly synthesize the compositions of ZIF-67 and cobalt nanocrystals by the strategy of *in-situ* NaBH$_4$ reduction during assembly of Co^{2+} and 2-methylimidazole. As schemed in Scheme 1, a ZIF-67 precursor was synthesized by assembling a small amount of Co^{2+} and an excess of 2-methylimidazole in the methanol

solution with stirring at room temperature for 30 min. Subsequently, a large amount of Co^{2+} and quantitative NaBH$_4$ were added to the above mixed solution. Benefiting from the rapid reduction of NaBH$_4$, the compositions of ZIF-67 and cobalt nanocrystals formed with a unique structure of Co nanocrystals wrapped in the continued growth of ZIF-67. Finally, the polyhedral carbon catalyst of Co$_3$O$_4$-Co@NC with a heterostructure Co$_3$O$_4$-Co NPs embedded in Co, N co-doped open carbon shell was achieved by high-temperature treatment of the collected purple powder under N$_2$ atmosphere. X-ray diffraction (XRD) patterns (Fig. S1 in the Electronic Supplementary Material (ESM)) and scanning electron microscopy (SEM) images (Fig. S2 in the ESM) of Co@ZIF-67 indicate that cobalt nanocrystals generated by *in-situ* NaBH$_4$ reduction did not significantly change the ZIF-67 crystallinities and zeolite-type structures. The SEM images in Figs. 1(a$_1$) and 1(b$_1$) exhibit that the size and polyhedral shapes of Co$_3$O$_4$-Co@NC-1 and Co$_3$O$_4$-Co@NC-2 are retained well after heat treatment, similar to the pure ZIF-67 derivative (Co@NC) (Fig. 1(d$_1$)), while the crystal structure of Co$_3$O$_4$-Co@NC-3 shrinks and collapses (Fig. 1(c$_1$)). The more clear morphological changes are observed in the transmission electron microscopy (TEM) as shown in Fig. S3 in the ESM, Figs. 1(a$_2$), 1(a$_3$), 1(d$_2$) and 1(d$_3$). The large-sized and uneven Co-based nanoparticles were distributed in sample Co$_3$O$_4$-Co@NC-1, while high density of smaller Co-based nanoparticles with narrow distribution was observed in Co$_3$O$_4$-Co@NC-2 (Figs. 1(b$_2$) and 1(b$_3$)). This finding suggests that the molar ratio of NaBH$_4$ to Co^{2+} plays the vital role in the morphology of nanomaterials derived from the compositions of ZIF-67 and cobalt nanocrystals. It is well-known that the Co atoms in ZIF-67 easily tend to diffuse and aggregate into large particles with nonuniform distribution due to decomposition of metal-imidazolate linkages during high-temperature pyrolysis [21]. For the compositions of ZIF-67 and cobalt nanocrystals prepared by our strategy of *in-situ* NaBH$_4$ reduction, the Co nanocrystals in the ZIF-67 hardly migrate during high-temperature pyrolysis due to the steric effect of metalimidazolate linkages around the Co nanocrystals. The Co atoms around the Co nanocrystals in the ZIF-67 migrate and react with Co nanocrystals to from Co-based NPs during high-temperature pyrolysis. Compared with Co$_3$O$_4$-Co@NC-1 with the NaBH$_4$/Co^{2+} molar ratio of 1, high density of smaller cobalt-based NPs on the Co$_3$O$_4$-Co@NC-2 is attributed to the formation of more nanocrystals in ZIF-67 when the NaBH$_4$/Co^{2+} molar ratio is 2. However, when the proportion of NaBH$_4$ continues to increase, two more Co nanocrystals formed in the compositions of ZIF-67 and cobalt nanocrystals destroy the basic structure of ZIF-67 during high-temperature pyrolysis, resulting in structural shrinkage and collapse (Figs. 1(c$_2$) and 1(c$_3$)). High-resolution TEM images in Figs. 1(a$_4$)–1(d$_4$)
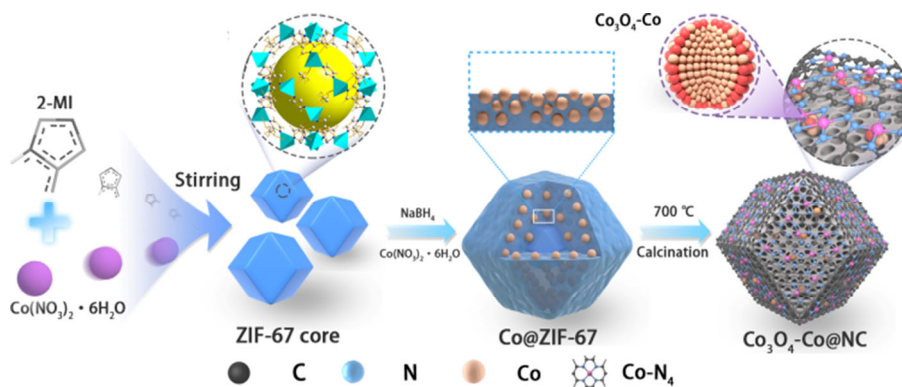
Scheme 1   Illustration of the preparation process of the Co$_3$O$_4$-Co@NC catalysts.
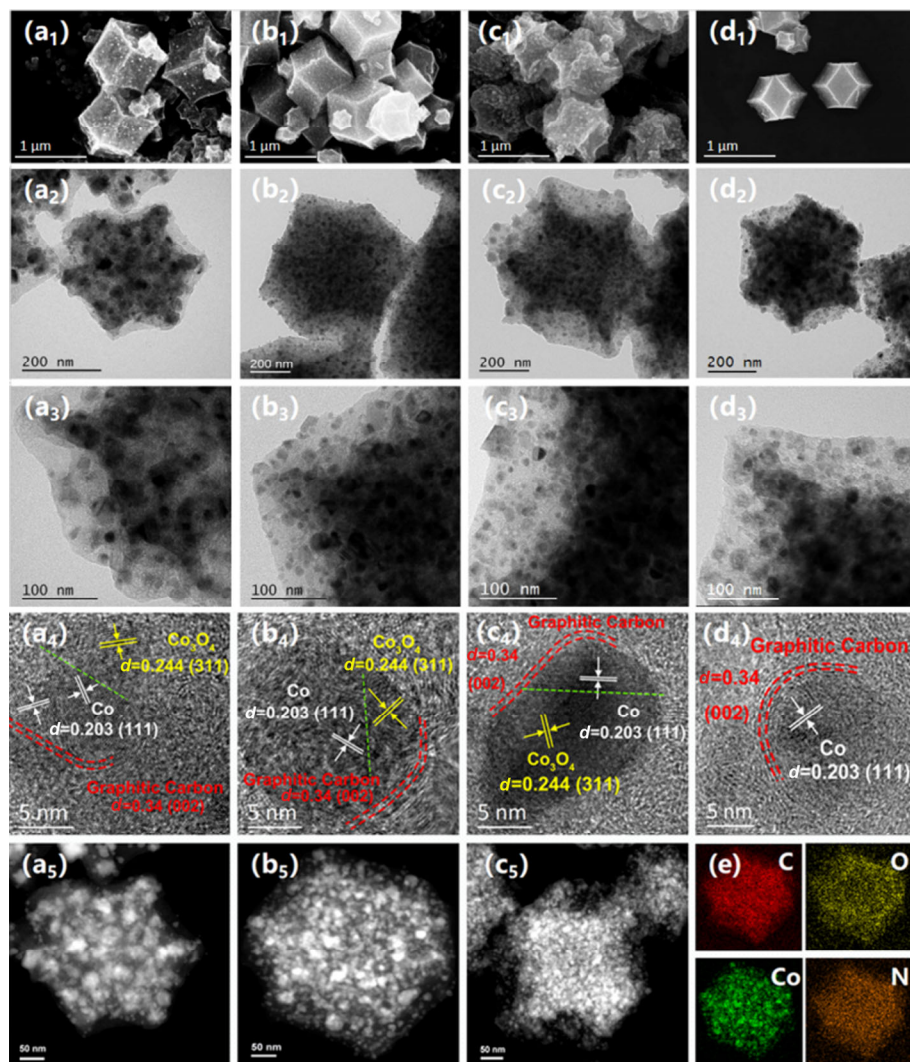
Figure 1   SEM, TEM, STEM and HRTEM images of various hybrids: (a1–a5) Co_3O_4-Co@NC-1; (b1–b5) Co_3O_4-Co@NC-2; (c1–c5) Co_3O_4-Co@NC-3; (d1–d4) Co@NC. (e) EDS mapping of Co_3O_4-Co@NC-2.

showed that discontinuous and open highly graphitized carbon skeleton (red line) closely contacts with Co-based nanoparticles, especially the Co_3O_4-Co@NC-2 (Fig. S4 in the ESM). Those discontinuous and open highly graphitized carbon graphitization are beneficial to favor electron and mass transfer by constructing an interconnected conductive network during the catalytic process. It's worth noting that only the cobalt NPs with ~ 0.203 nm well-defined lattice fringes were observed in Co@NC (Fig. 1(d4)), which matches the (111) planes of face-centered cubic (fcc) metallic cobalt [34]. After $NaBH_4$ was added, another lattice with a lattice spacing of ~ 0.244 nm appears in all Co_3O_4-Co@NC (Figs. 1(a4)–1(c4)), which belongs to the (311) planes of spinel Co_3O_4 [35]. In addition, a distinct biphasic interface was observed between metal Co and Co_3O_4 in all Co_3O_4-Co@NC, highlighted by the green dashed line. This formation of the interpenetrating heterointerfaces at the atomic-scale facilitates charge separation, resulting in effectively capturing more oxygen intermediates and favoring charge transfer within the active site [36, 37]. The powder XRD in Fig. 2(a) also indicates a clear fcc metallic cobalt (JCPDS No. 15-0806) in Co@NC with the peaks located at 44.3°, 51.5° and 75.9°, corresponding to the (111), (200), and (220) planes of metallic cobalt, respectively. In contrast, after introducing $NaBH_4$, these peaks become wider and weaker in the pattern of Co_3O_4-Co@NC-2 and Co_3O_4-Co@NC-3, suggesting that our $NaBH_4$ strategy leads to the formation of small Co-base

NPs during high-temperature pyrolysis of ZIF-67. These results suggest that our strategy of *in-situ* $NaBH_4$ reduction not only effectively facilitates the formation of Co_3O_4-Co, but also adjusts the size of Co_3O_4-Co NPs in ZIF-67 derived carbon nanocatalyst. The well-tuned Co_3O_4-Co NPs in ZIF-67 derived carbon nanocatalyst has been proved to possess high bifunctional catalytic activities towards the OER/ORR [36, 38]. The additional weak peak at about 36.8° in Co_3O_4-Co@NC-2 and Co_3O_4-Co@NC-3 should arise from the (311) planes of Co_3O_4 (JCPDS No. 43-1003). The homogeneous C, O, Co and N elements were observed in the energy dispersive X-ray spectrocscopy (EDS) mappings (Fig. 1(e)) of Co_3O_4-Co@NC-2. The corresponding elemental mass fraction was listed Fig. S5 and Table S1 in the ESM. The Raman spectrum of Co_3O_4-Co@NC-2, as shown in Fig. 2(b), indicates the relative ratio (I_D/I_G) of D and G bands at 1,350 and 1,588 cm^{-1} is 1.03, higher than Co_3O_4-Co@NC-1 (1.02) and Co@NC (1.00). The higher I_D/I_G value should be attributed to the more defects [39], which is highly favorable for oxygen catalysis by enhancing the O_2 adsorption capability [40]. Besides, a minor peak at 671 cm^{-1} can be attributed to the A_{1g} vibration mode of Co_3O_4 in these samples [41, 42].

The surface electronic properties of four calcined catalysts were measured by X-ray photoelectron spectroscopy (XPS) as shown in Fig. S6 and Table S2 in the ESM. The deconvolution of high-resolution N 1s spectra (Fig. 2(c)) is further obtained with five types of nitrogen species: pyridinic N (398.3 eV),
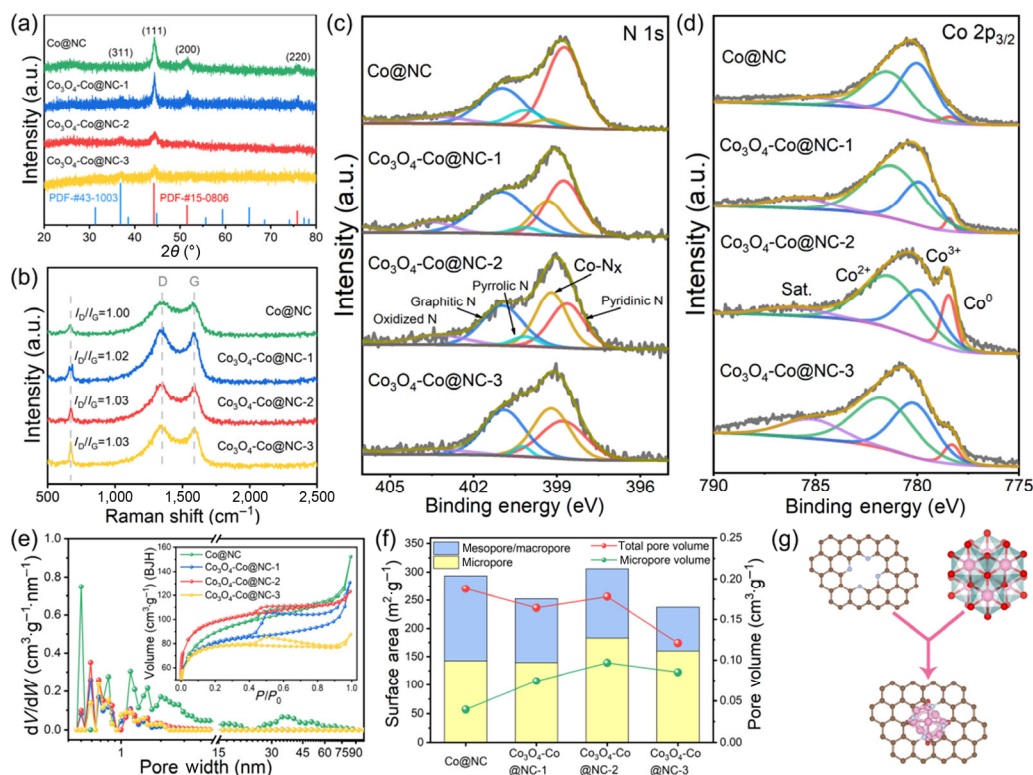
Figure 2 (a) XRD patterns. (b) Raman spectra. (c) N 1s high-resolution XPS spectra. (d) Co 2p high-resolution XPS spectra. (e) Pore size distributions and nitrogen adsorption-desorption isotherms (the inset) and (f) BET surface area and pore volume of pores of various samples. (g) Schematic diagram of the model combining Co_3O_4-Co nanoparticles and carbon layers.

Co-N bonding (399.2 eV), graphitic N (400.8 eV), pyrrolic N (400.2 eV) and oxidated N (403-406 eV) [37, 43–46]. It is worth noting that Co_3O_4-Co@NC-2 has a higher proportion of Co-N and pyridine-N, especially compared with Co@NC (Table S3 in the ESM), which was proved to be the highly efficient ORR active sites [47–50]. This finding indicates that our strategy of *in-situ* $NaBH_4$ reduction can effectively increase the active sites of Co-N$_x$ in ZIF-67 derived carbon nano-catalyst. Moreover, the main peaks of N 1s of Co_3O_4-Co@NC samples show about 0.4 eV positive shift compared to that of Co@NC (Fig. S7 in the ESM), resulting from the strong electron-withdrawing effect of Co in Co-N$_x$-C moieties on Co_3O_4-Co@NC catalyst [24]. The high-resolution Co 2p XPS spectra of all samples shows three cobalt species: Co^0 (778.4 eV), Co^{3+} (779.9 eV) and Co^{2+} (781.3 eV) [37, 51–54], indicating the co-existence of Co_3O_4 and metallic Co species. Additionally, the percentage of the metallic Co phase is 2.51% for Co@NC, 3.62% for Co_3O_4-Co@NC-1, 12.77% for Co_3O_4-Co@NC-2 and 5.32% for Co_3O_4-Co@NC-3 (Table S4 in the ESM). The low Co^0 content of Co_3O_4-Co@NC-3 probably results from the polyhedral skeleton contraction and collapse in the high-temperature pyrolysis process, which leads to cobalt nanoparticles in Co_3O_4-Co@NC-3 agglomeration into larger size than Co_3O_4-Co@NC-2. Clearly, the atom ratio of Co^{2+}/Co^{3+} of Co_3O_4-Co@NC-1 (1.67), Co_3O_4-Co@NC-2 (1.57) and Co_3O_4-Co@NC-3 (1.28) are much higher than Co@NC (0.94). The higher Co^{2+}/Co^{3+}atomic ratio suggests the formation of relatively more oxygen vacancies, which further confirmed by the high-resolution O 1s XPS spectra (Fig. S8 and Table S5 in the ESM).

The porosity of all catalysts was further evaluated by N_2 ad/desorption measurements (the inset of Fig. 2(e)). All samples showed typical type-IV isotherms, which indicated the presence of micropores and mesopores. The pore size distribution curve in Fig. 2(e) shown that Co_3O_4-Co@NC

samples has more abundant micropore size than Co@NC. In addition, with the increase of $NaBH_4$ addition, the surface area of the series samples presents a trend first increases and then decreases. Co_3O_4-Co@NC-2 shows the highest surface area of 306.2 $m^2·g^{-1}$, larger than that of Co_3O_4-Co@NC-1 (252.6 $m^2·g^{-1}$) and Co_3O_4-Co@NC-3 (237.4 $m^2·g^{-1}$), but close to the Co@NC (293.4 $m^2·g^{-1}$) (Table S6 in the ESM). The low specific surface area of Co_3O_4-Co@NC-3 maybe due to the collapse and shrinkage of the structure of nanomatrials derived the compositions of ZIF-67 and excessive cobalt nanocrystals, as shown in SEM images (Fig. 1(c$_1$)). By comparing the surface area and pore volume of different types of pores in Fig. 2(f) and Table S7 in the ESM, we found that the micropores pore volume of Co_3O_4-Co@NC increase with *in situ* addition $NaBH_4$, especially Co_3O_4-Co@NC-2 (54%), which are much higher than Co@NC (21%). These results indicate that the in situ $NaBH_4$ reduction strategy can create more micropores in ZIF-67 derived nanomaterials. A large number of micropores facilitate exposing more active sites and mass transfer (Co-N$_x$/Co_3O_4-Co) (Fig. 2(g)), leading to the increase in the electrochemical activity.

To evaluate the electrocatalytic performance of Co_3O_4-Co@NC, ORR were first investigated using the linear sweep voltammetry (LSV) in O_2-saturated 0.1 M KOH solution. As shown in Fig. 3(a)**,** the Co_3O_4-Co@NC-2 exhibits superior ORR activity with an onset potential and half-wave potential at 0.97 and 0.86 V, respectively, which is better than those of Co_3O_4-Co@NC-1 (0.94 and 0.85 V), Co_3O_4-Co@NC-3 (0.91 and 0.82 V) and Co@NC (0.91 and 0.82 V), very closely to commercial Pt/C (1.00 and 0.87 V). As shown in Fig. 3(b)**,** Co_3O_4-Co@NC-2 possesses the smallest Tafel slope of ~ 72 $mV·dec^{-1}$, smaller than that of Co_3O_4-Co@NC-1 (75 $mV·dec^{-1}$), Co_3O_4-Co@NC-3 (78 $mV·dec^{-1}$), Co@NC (82 $mV·dec^{-1}$), commercial Pt/C (86 $mV·dec^{-1}$), suggesting its favorable reaction kinetics. The rotating ring-disk electrode (RRDE) measurement (Fig. 3(c))
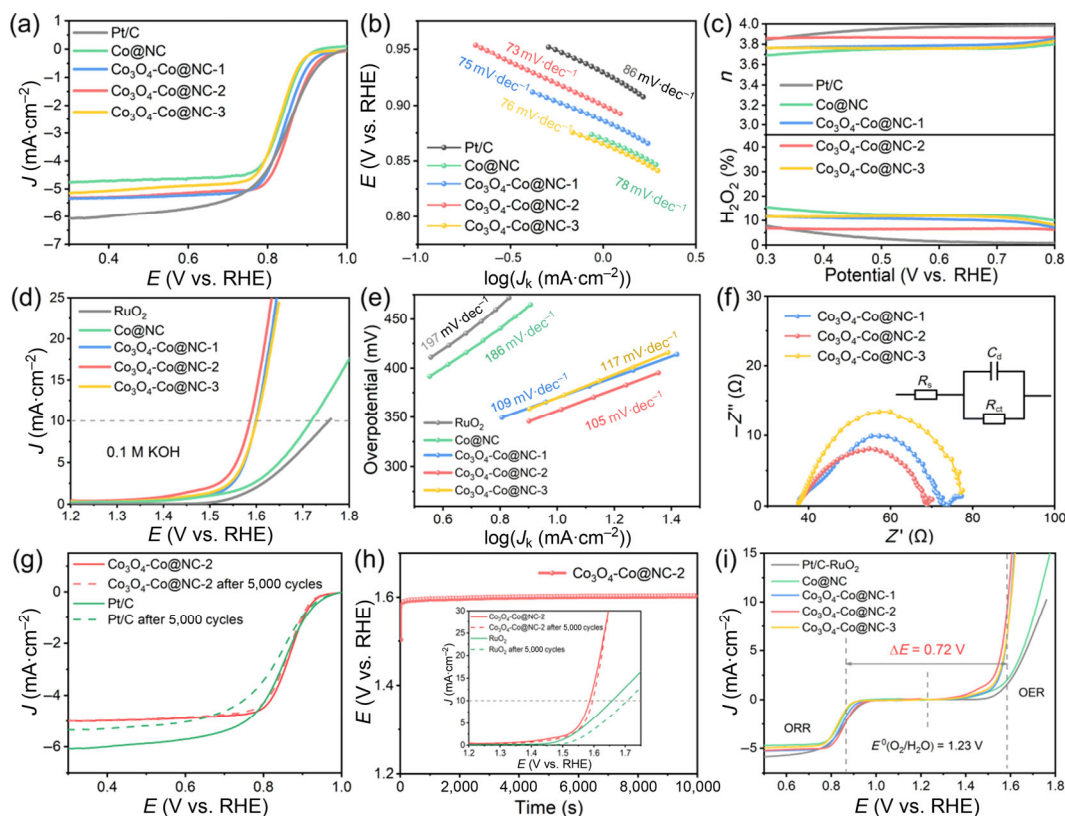
Figure 3 (a) ORR polarization curves. (b) The corresponding Tafel plots for ORR. (c) Peroxide yields (HO_2^-%) and electron transfer numbers (n) of various catalysts. (d) OER polarization curves. (e) The corresponding Tafel plots for OER, (f) Nyquist plots, (g) LSV curves of the Co_3O_4-Co@NC-2 catalyst before and after 5,000 cycles in 0.1 M KOH for ORR, (h) OER time-dependent stability by chronoamperometric response at a constant current density of 10 mA·cm^{-2} for 10,000 s and LSV curves before and after 5,000 cycles in 0.1 M KOH for OER (the inset) of the Co_3O_4-Co@NC-2 catalyst. (i) Combined ORR/OER polarization curves of various catalysts in O_2-saturated 0.1 M KOH electrolyte (rotation rate: 1,600 rpm; scan rate: 5 mV·s^{-1}).

also confirmed that the Co_3O_4-Co@NC-2 has high ORR activity with low HO_2^- yield (below 10%) and an n value of 3.8–3.85, higher than that of others catalysts and approaching to the value of Pt/C. This finding indicates four-electron transfer pathway on Co_3O_4-Co@NC-during ORR process, which is also confirmed by the K-L plots of ring-disk electrode (RDE) measurements (Fig. S9 in the ESM). For practical applications, the stability is another critical factor. The electrochemical stability tests show in Fig. 3(g) that the half-wave potential of Co_3O_4-Co@NC-2 catalyst is almost no negative shift (< 5 mV) after 5,000 cyclic voltammetry (CV) cycling, much better than commercial Pt/C catalyst, indicating the excellent durability in an alkaline medium. The Co_3O_4-Co@NC-2 catalyst also indicates good cross-tolerance to methanol (Fig. S10 in the ESM), showing an excellent selectivity for ORR.

The OER activities of Co_3O_4-Co@NC samples are also measured in O_2-saturated 0.1 M KOH solution. The OER polarization curve (Fig. 3(d)) displays that Co_3O_4-Co@NC-2 requires a much small overpotential of only 350 mV to approach 10 mA·cm^{-2}, lower than commercial RuO_2 (530 mV), Co_3O_4-Co@NC-1 (368 mV), Co_3O_4-Co@NC-3 (370 mV), Co@NC (490 mV). The corresponding Tafel plots (Fig. 3(e)) with calculated by fitting LSV also shown that Co_3O_4-Co@NC-2 has the smallest Tafel slope (105 mV·dec^{-1}) among four catalysts, lower than Co_3O_4-Co@NC-1 (109 mV·dec^{-1}), Co_3O_4-Co@NC-3 (117mV·dec^{-1}), Co@NC (186mV·dec^{-1}) and RuO_2 (197 mV·dec^{-1}). Co_3O_4-Co@NC-2 shows manifesting its favorable OER kinetics. Figure S11 in the ESM shows that the double-layer capacitance (C_{dl}) value of Co_3O_4-Co@NC-2 (20.6 mF·cm^{-2}) is higher than those of Co_3O_4-Co@NC-1 (19.6 mF·cm^{-2}) and Co_3O_4-Co@NC-3 (17.7 mF·cm^{-2}), suggesting Co_3O_4-Co@NC-2 has more exposed active sites, which is well consistent with N_2 ad/desorption

results. As shown in Fig. 3(f) and Table S8 in the ESM, the Co_3O_4-Co@NC-2 has the smallest charge transfer resistance (31.2 Ω) in comparison with Co_3O_4-Co@NC-1 (34.3 Ω) and Co_3O_4-Co@NC-3 (40.5 Ω), indicating high charge transfer rate and kinetic activity on Co_3O_4-Co@NC-2. In addition, as shown in Fig. S12 in the ESM, the TOF value of Co_3O_4-Co@NC-2 was 0.013 s^{-1}, which was much higher than Co@NC (0.002 s^{-1}) derived from pure ZIF-67, indicating that Co_3O_4-Co@NC-2 contains more catalytic active sites than Co@NC. Most importantly, Co_3O_4-Co@NC-2 shows an excellent OER stability with small ΔE (< 5 mV) after 5,000 cycles, lower than RuO_2 ($\Delta E \approx 30$ mV) (inset Fig. 3(h)). The chronoamperometric measurement as shown in Fig. 3(h) further verifies an excellent stability on Co_3O_4-Co@NC-2. The potential gap ($\Delta E = E_{j=10}$ (OER) $- E_{1/2}$(ORR)) was performed to further elucidate the bifunctional catalytic activity. The smaller ΔE indicates that the superior bifunctional catalytic activity [55]. As illustrated in Fig. 3(i), Co_3O_4-Co@NC-2 exhibits the smallest ΔE value of 0.72 V among the as-prepared catalysts, which much better than noble metal (Pt/C-RuO_2) benchmarks ($\Delta E = 0.77$ V). More importantly, the above excellent bifunctional performance makes Co_3O_4-Co@NC-2 to be one of the outstanding bifunctional catalysts (Table S9 in the ESM).

The determination of the active site is very important to design/develop high performance of bifunctional catalysts. The XRD pattern in Fig. 13(a) shows that after acid leaching, the peak of 36.5° corresponding to Co_3O_4 (311) plane almost disappears and the peak of 44.3° corresponding to Co(111) plane significantly decreases, indicating that Co_3O_4 and Co nanoparticles in Co_3O_4-Co@NC-2 were etched by H_2SO_4 solution. As shown in Figs. S13(b) and S13(c) in the ESM, after H_2SO_4 solution leaching, the ORR and OER catalytic

performance of the Co₃O₄-Co@NC-2 deteriorated significantly, indicating that Co_3O_4 and Co nanoparticles contributed main bifunctional electrocatalytic activity. However, Co₃O₄-Co@NC-2 still retained considerable ORR and OER catalytic activity after acid leaching, indicating that Co-N$_x$ sites also contributed certain catalytic activity. Therefore, the outstanding ORR and OER performances of Co₃O₄-Co@NC-2 results from the synergistic effect between the dual active sites of Co-N$_x$ and Co₃O₄-Co nanoparticles adjusted by *in-situ* NaBH₄ reduction. Furthermore, as shown in Fig. S14 in the ESM, a pyrolysis temperature gradient examination (600, 700, 800 and 900 ℃) showed that the Co₃O₄-Co@NC-2 obtained at 700 ℃ had the highest ORR/OER catalytic activity, due to the optimized nanoparticles size at 700 ℃ pyrolysis temperature.

The density functional theory (DFT) calculations were performed to explore the synergistic effect between the dual active sites of Co-N$_x$ and Co₃O₄-Co nanoparticles for enhancing reversible ORR/OER activities. According to the previous studies [56, 57], the high-speed conversion of intermediate molecules on the Co-N₄ site in the catalytic reaction exhibits its high intrinsic oxygen catalytic activity. In addition, cobalt oxide has a greater regulatory effect on the process of catalysing the evolution of oxygen due to the coupling of the electron orbits of cobalt and oxygen [58, 59]. In this work, the Co₃O₄-Co nanoparticles were wrapped by the carbon layer containing Co-N$_x$ moieties in Co₃O₄-Co@NC-2 according to TEM and XPS results. Therefore, the Co metal cluster and Co-O cluster anchored at the Co-N₄ site in the single-layer carbon network are modelled [60], respectively, to identify the critical role of Co-O in affecting the ORR/OER energetics of Co₃O₄-Co@NC-2 [61]. As shown in Figs. 4(a₁) and 4(a₂)), the significant interfacial electron transfer from the metal/metal oxide cluster to the Co-N₄ in the Co-O/Co-N₄-C hybrid resulted in electron deletion region on the CoO surface and electron accumulation on the Co-N₄ surface, which was consistent with the XPS results. Moreover, compared with Co/Co-N₄-C (Fig. S15 in the ESM), it is obvious that more

charge accumulated at the center of the Co-N₄ active site of Co-O/Co-N₄-C, which provides more electrons to participate in electrochemical catalysis. This result suggests that the synergistic effect of Co-O nanoparticles and Co-N₄ active site on our Co₃O₄-Co@NC-2 provide more electrons from both nitrogen atoms and Co-O nanoparticles (Figs. 4(a₃)and 4(a₄)), which is beneficial for optimizing the adsorption of O₂ or OH⁻ and the corresponding intermediates and thus favoring the reversible ORR/OER processes [60, 62]. The projected density of states (DOS) of all three catalysts shown in Fig. 4(b), compared with Co/Co-N₄-C, the d-band center of Co in Co-O/Co-N₄-C undergoes a negative shift of 0.2 eV (from 1.09 to 1.29 eV) relative to the Fermi level due to the coupling of the d orbital electron of Co and the p orbital electron of O, resulting in the peaks formed by the increase of charge density between −4 and −7 eV. According to the d-band center theory [63, 64], this will reduce the energy of the anti-bond state and increases the filling rate of the d orbital, resulting in weaker bonding strength, thus improves the adsorption and desorption of O₂ and OH⁻, and accelerates the reaction kinetics of ORR and OER. Based on previous studies [65–67], the ORR kinetic process under alkaline conditions includes four parts: the thermodynamic adsorption of oxygen (O₂*) and the electro-chemical reactions of the continuous evolution through the formation of HOO*, O*, and HO*, as shown in Fig. 4(c) and Figs. S16–S18 in the ESM, and the OER occurs in the reverse direction. Moreover, the overall ORR/OER free energy diagram at the equilibrium potential (U^0_{RHE} = 1.23 V) in Fig. 4(d) shows that the rate-limiting steps for Co-N$_x$ models are focused on the desorption process, that is, OH⁻ desorption in the ORR process and O₂ desorption in the OER process. Due to the strong chemical adsorption of O₂, it becomes quite difficult for Co-N₄ active site to the subsequent desorption behavior (ΔG_{OO^*} = 0.82 eV and ΔG_{OH^*} = 0.63 eV), which hinders the utilization efficiency of the active site and leads to the sluggish reaction kinetic. On the contrary, when combined Co-N₄ with Co and Co-O nanoparticles, respectively, the reaction barriers
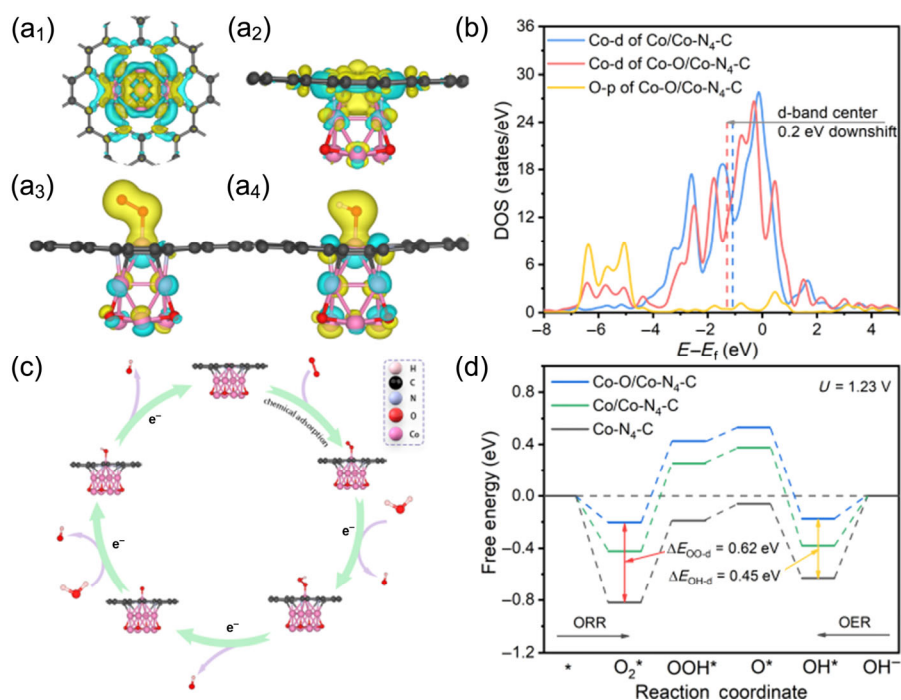
Figure 4 Isosurface of charge density variation in (a₁) and (a₂) Co-O/Co-N₄-C and (a₃) and (a₄) O₂ and OH⁻ are adsorbed on the Co-N₄ active site of Co-O/Co-N₄-C. Green area denotes charge density decrease ($\Delta\rho < 0$) and yellow area denotes charge density increase ($\Delta\rho > 0$). (b) The projected density of states of Co-N₄-C, Co/Co-N₄-C and Co-O/Co-N₄-C. (c) Schematic diagram of ORR kinetic process occurring on the surface of catalytic model in alkaline medium. (d) The free energy diagrams of ORR and OER at the equilibrium potential on various catalysts.

of $\Delta G_{O_2^*}$ and ΔG_{OH^*} in Co/Co-N$_4$-C and Co-O/Co-N$_4$-C are largely reduced, especially Co-O/Co-N$_4$-C ($\Delta E_{OO-d} = 0.62$ eV and $\Delta E_{OH-d} = 0.45$ eV), which weakens the bond strength between the Co-N$_4$ active sites and the adsorbed molecule (Fig. S19 in the ESM), and improves the subsequent desorption step. In this case, the formation of OOH* (ORR) and O* (OER) are rate-limiting steps for Co/Co-N$_4$-C and Co-O/Co-N$_4$-C, and the corresponding overpotentials are significantly decreased compared with pure Co-N$_4$. The overpotential trend of all three different catalysts follows the order of Co-N$_4$ (0.82 V) > Co/Co-N$_4$-C (0.74 V) > Co-O/Co-N$_4$-C (0.71 V) (Fig. S20 in the ESM). Therefore, benefitting from the tuning cobalt-based active sites of Co-O nanoparticles and Co-N$_4$ on our Co$_3$O$_4$-Co@NC-2, the adsorption and desorption characteristics of all oxygen intermediates on the Co site of Co-N$_4$ were greatly promoted, thus optimizing the reaction path and accelerating the reaction kinetics. In summary, the DFT calculations, in consistent with experimental results, highlight the the synergistic effects of well-tuned dual-active sites of Co$_3$O$_4$-Co nanoparticle and Co-N$_x$ in our Co$_3$O$_4$-Co@NC-2 to produce a optimizing surface electronic environment and thereby enhancing ORR/OER performance.

A rechargeable liquid ZABs was fabricated with the Co$_3$O$_4$-Co@NC-2 catalyst as the cathode electrode (Fig. 5(a)) to verify its practical application. As illustrated in Fig. 5(b), the assembled ZABs afforded a higher open-circuit voltage of 1.46 V, better than the Pt/C-RuO$_2$ based ZABs (1.43 V). The charge and discharge curves of electrodes with Co$_3$O$_4$-Co@NC-2 in Fig. 5(c) display a smaller charge-discharge voltage gap relative to Pt/C-RuO$_2$, exhibiting superior reversible oxygen electrode catalytic activity. The discharge polarization (V–j)

curve and corresponding power density of ZABs equipped with Co$_3$O$_4$-Co@NC-2 catalyst were revealed in Fig. 5(d), displaying the excellent peak-power density of 158 mW·cm^{-2}, two times greater than ZABs with Pt/C-RuO$_2$ (79 mW·cm^{-2}). In addition, a voltage platform of 1.22 V was observed on the ZABs with the Co$_3$O$_4$-Co@NC-2 at 20 mA·cm^{-2}, (Fig. 5(e)), much higher that Pt/C+RuO$_2$ (1.09 V). The high specific capacity (758 mAh·g$_{Zn}^{-1}$) and energy density (924 Wh·kg$_{Zn}^{-1}$) were achieved for Co$_3$O$_4$-Co@NC-2, greater than Pt/C+RuO$_2$ (617 mAh·g$_{Zn}^{-1}$ and 654 Wh·kg$_{Zn}^{-1}$). Notably, the Co$_3$O$_4$-Co@NC-2 electrocatalyst exhibits the discharging voltage at 20 mA·cm^{-2} is as high as 1.10 V (Fig. 5(f)), indicating the excellent high-rate performance. The durability of the Co$_3$O$_4$-Co@NC-2 cathode for the Zn-air battery was further proved by galvanostatic discharge-charge long cycling at 10 mA·cm^{-2}. As illustrated in Fig. 5(g), the initial charge-discharge voltage gap on the ZAB equipped by Co$_3$O$_4$-Co@NC-2 is 1.2 V, smaller than the Pt/C+RuO$_2$ catalyst (1.65 V). More importantly, after 200 cycles of testing, the Co$_3$O$_4$-Co@NC-2 air cathodes display a slight performance loss with only 0.17 V increase, whereas the battery with Pt/C+RuO$_2$ catalyst shows a poor cyclability with less than 30 h. From these results, compared with noble metal-based catalysts, the Co$_3$O$_4$-Co@NC-2 air cathode exhibits excellent performance as a reversible oxygen electrode in a rechargeable ZAB.

3 Conclusions

In summary, the Co$_3$O$_4$-Co NPs encapsulated in co, N Co-doped open carbon shell through tuning the dual-Co-based active sites and internal pore structure of carbon nanomaterial derived from ZIF-67 is prepared by *in-situ* NaBH$_4$ reduction.
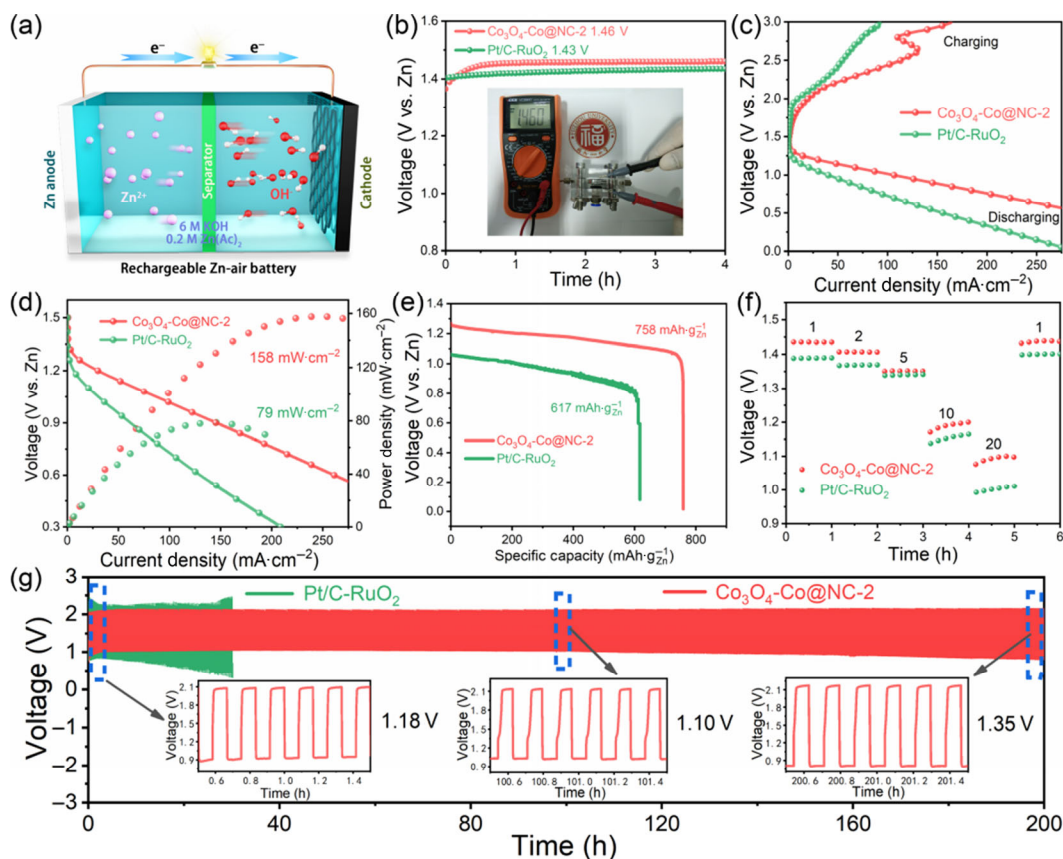

Figure 5 Fabrication and performance of Co$_3$O$_4$-Co@NC-2 based ZABs. (a) Schematic of rechargeable ZABs. (b) Open-circuit plots and photograph of Co$_3$O$_4$-Co@NC-2 based ZAB exhibiting a high open-circuit voltage of ≈ 1.46 V. (c) Charge and discharge polarization (V–j) curves. (d) Discharge polarization (V–j) curves and the corresponding power density curves. (e) Specific capacities plots at 20 mA·cm^{-2}. (f) Discharge curves at various discharge current densities. (g) Galvanostatic discharge-charge cycling curves at 10 mA·cm^{-2} of rechargeable Co$_3$O$_4$-Co@NC-2 based ZABs.

This strategy creates the small size heterogeneous Co_3O_4-Co nanoparticles and coupled with Co-N_x sites in the porous carbon shell to increase the bifunctional catalytic activity. The designed Co_3O_4-Co@NC shows excellent OER/HER bifunctional electrocatalytic activity and stability, outperforming the commercial Pt/C and RuO_2 catalysts. DFT calculation reveals that the electron coupling between Co-O and Co-N_4 causes a negative shift of the d-band center of Co adsorption site in Co-N_4, which greatly reduces the energy barrier of oxygen-containing intermediate O_2^* in ORR and OH* in OER process and accelerates the overall ORR/OER catalytic process. This work provides a new inspiration to rationally design high-performance non-noble metal catalysts by tuning the active site for energy conversion and storage applications.

Acknowledgements

Electronic Supplementary Material: Supplementary material (further details of experimental and computation methods, additional TEM images, EDX spectrum, XPS spectra, BET data, electrochemical activities and theoretical simulation analysis of relevant samples) is available in the online version of this article at https://doi.org/10.1007/s12274-020-3234-6.

References

[1]   Li, Y. G.; Dai, H. J. Recent advances in zinc-air batteries. *Chem. Soc. Rev.* **2014**, *43*, 5257–5275.

[2]   Lei, W.; Deng, Y. P.; Li, G. R.; Cano, Z. P.; Wang, X. L.; Luo, D.; Liu, Y. S.; Wang, D. L.; Chen, Z. W. Two-dimensional phosphorus-doped carbon nanosheets with tunable porosity for oxygen reactions in zinc-air batteries. *ACS Catal.* **2018**, *8*, 2464–2472.

[3]   Wu, M. J.; Zhang, G. X.; Wu, M. H.; Prakash, J.; Sun, S. H. Rational design of multifunctional air electrodes for rechargeable Zn–air batteries: Recent progress and future perspectives. *Energy Storage Mater.* **2019**, *21*, 253–286.

[4]   Li, M.; Bi, X. X.; Wang, R. Y.; Li, Y. B.; Jiang, G. P.; Li, L.; Zhong, C.; Chen, Z. W.; Lu, J. Relating catalysis between fuel cell and metal-air batteries. *Matter* **2020**, *2*, 32–49.

[5]   Wang, Y. J.; Fang, B. Z.; Zhang, D.; Li, A. J.; Wilkinson, D. P.; Ignaszak, A.; Zhang, L.; Zhang, J. J. A review of carbon-composited materials as air-electrode bifunctional electrocatalysts for metal–air batteries. *Electrochem. Energy Rev.* **2018**, *1*, 1–34.

[6]   Lai, C. L.; Gong, M. X.; Zhou, Y. C.; Fang, J. Y.; Huang, L.; Deng, Z. P.; Liu, X. P.; Zhao, T. H.; Lin, R. Q.; Wang, K. L. et al. Sulphur modulated Ni_3FeN supported on N/S co-doped graphene boosts rechargeable/flexible Zn-air battery performance. *Appl. Catal. B Environ.* **2020**, *274*, 119086.

[7]   Li, Y. G.; Zhou, W.; Wang, H. L.; Xie, L. M.; Liang, Y. Y.; Wei, F.; Idrobo, J. C.; Pennycook, S. J.; Dai, H. J. An oxygen reduction electrocatalyst based on carbon nanotube-graphene complexes. *Nat. Nanotechnol.* **2012**, *7*, 394–400.

[8]   Guan, C.; Sumboja, A.; Wu, H. J.; Ren, W. N.; Liu, X. M.; Zhang, H.; Liu, Z. L.; Cheng, C. W.; Pennycook, S. J.; Wang, J. Hollow Co_3O_4 nanosphere embedded in carbon arrays for stable and flexible solid-state zinc-air batteries. *Adv. Mater.* **2017**, *29*, 1704117.

[9]   Amiinu, I. S.; Liu, X. B.; Pu, Z. H.; Li, W. Q.; Li, Q. D.; Zhang, J.; Tang, H. L.; Zhang, H. N.; Mu, S. C. From 3D ZIF nanocrystals to Co-N_x/C nanorod array electrocatalysts for ORR, OER, and Zn-air batteries. *Adv. Funct. Mater.* **2018**, *28*, 1704638.

[10] Li, Y. H.; Li, Q. Y.; Wang, H. Q.; Zhang, L.; Wilkinson, D. P.; Zhang, J. J. Recent progresses in oxygen reduction reaction electrocatalysts for electrochemical energy applications. *Electrochem. Energy Rev.* **2019**, *2*, 518–538.

[11] Wu, G.; Zelenay, P. Nanostructured nonprecious metal catalysts for oxygen reduction reaction. *Acc. Chem. Res.* **2013**, *46*, 1878–1889.

[12] Feng, T.; Zhao, X. R.; Dong, C. K.; Liu, H.; Du, X. W.; Yang, J. Boosting reversible oxygen electrocatalysis with enhanced interfacial pyridinic-N–Co bonding in cobalt oxide/mesoporous N-doped graphene hybrids. *Nanoscale* **2018**, *10*, 22140–22147.

[13] Wei, Q. L.; Zhang, G. X.; Yang, X. H.; Fu, Y. Q.; Yang, G. H.; Chen, N.; Chen, W. F.; Sun, S. H. Litchi-like porous Fe/N/C spheres with atomically dispersed FeN_x promoted by sulfur as highly efficient oxygen electrocatalysts for Zn–air batteries. *J. Mater. Chem. A* **2018**, *6*, 4605–4610.

[14] Lai, C. L.; Wang, J.; Lei, W.; Xuan, C. J.; Xiao, W. P.; Zhao, T. H.; Huang, T.; Chen, L. X.; Zhu, Y.; Wang, D. L. Restricting growth of Ni_3Fe nanoparticles on heteroatom-doped carbon nanotube/graphene nanosheets as air-electrode electrocatalyst for Zn–air battery. *ACS Appl. Mater. Interfaces* **2018**, *10*, 38093–38100.

[15] She, Y. Y.; Liu, J.; Wang, H. K.; Li, L.; Zhou, J. S.; Leung, M. K. H. Bubble-like Fe-encapsulated N,S-codoped carbon nanofibers as efficient bifunctional oxygen electrocatalysts for robust Zn–air batteries. *Nano Res.* **2020**, *13*, 2175–2182.

[16] Tan, Y. Y.; Zhang, Z. Y.; Lei, Z.; Wu, W.; Zhu, W. B.; Cheng, N. C.; Mu, S. C. Thiourea-zeolitic imidazolate Framework-67 assembly derived Co–CoO nanoparticles encapsulated in N, S codoped open carbon shell as bifunctional oxygen electrocatalyst for rechargeable flexible solid Zn–air batteries. *J. Power Sources* **2020**, *473*, 228570.

[17] Zhu, B. J.; Liang, Z. B.; Xia, D. G.; Zou, R. Q. Metal-organic frameworks and their derivatives for metal–air batteries. *Energy Storage Mater.* **2019**, *23*, 757–771.

[18] Yang, L.; Zeng, X. F.; Wang, W. C.; Cao, D. P. Recent progress in MOF-derived, heteroatom-doped porous carbons as highly efficient electrocatalysts for oxygen reduction reaction in fuel cells. *Adv. Funct. Mater.* **2018**, *28*, 1704537.

[19] Wang, J.; Wang, Y. L.; Hu, H. B.; Yang, Q. P.; Cai, J. J. From metal–organic frameworks to porous carbon materials: Recent progress and prospects from energy and environmental perspectives. *Nanoscale* **2020**, *12*, 4238–4268.

[20] Wu, X.; Meng, G.; Liu, W. X.; Li, T.; Yang, Q.; Sun, X. M.; Liu, J. F. Metal-organic framework-derived, Zn-doped porous carbon polyhedra with enhanced activity as bifunctional catalysts for rechargeable zinc–air batteries. *Nano Res.* **2018**, *11*, 163–173.

[21] Cheng, N. Y.; Ren, L.; Xu, X.; Du, Y.; Dou, S. X. Recent development of zeolitic imidazolate frameworks (ZIFs) derived porous carbon based materials as electrocatalysts. *Adv. Energy Mater.* **2018**, *8*, 1801257.

[22] Guo, J.; Gadipelli, S.; Yang, Y. C.; Li, Z. N.; Lu, Y.; Brett, D. J. L.; Guo, Z. X. An efficient carbon-based ORR catalyst from low-temperature etching of ZIF-67 with ultra-small cobalt nanoparticles and high yield. *J. Mater. Chem. A* **2019**, *7*, 3544–3551.

[23] Fu, Y. Q.; Wei, Q. L.; Zhang, G. X.; Wang, X. M.; Zhang, J. H.; Hu, Y. F.; Wang, D. N.; Zuin, L.; Zhou, T.; Wu, Y. C. et al. High-performance reversible aqueous Zn-ion battery based on porous MnO_x nanorods coated by MOF-derived N-doped carbon. *Adv. Energy Mater.* **2018**, *8*, 1801445.

[24] Tang, C.; Wang, B.; Wang, H. F.; Zhang, Q. Defect engineering toward atomic Co-N_x-C in hierarchical graphene for rechargeable flexible solid Zn–air batteries. *Adv. Mater.* **2017**, *29*, 1703185.

[25] Chen, Z. L.; Ha, Y.; Jia, H. X.; Yan, X. X.; Chen, M.; Liu, M.; Wu, R. B. Oriented transformation of Co-LDH into 2D/3D ZIF-67 to achieve Co-N-C hybrids for efficient overall water splitting. *Adv. Energy Mater.* **2019**, *9*, 1803918.

[26] He, Y. H.; Hwang, S.; Cullen, D. A.; Uddin, M. A.; Langhorst, L.; Li, B. Y.; Karakalos, S.; Kropf, A. J.; Wegener, E. C.; Sokolowski, J. et al. Highly active atomically dispersed CoN_4 fuel cell cathode catalysts derived from surfactant-assisted MOFs: Carbon-shell confinement strategy. *Energy Environ. Sci.* **2019**, *12*, 250–260.

[27] Lei, Z.; Tan, Y. Y.; Zhang, Z. Y.; Wu, W.; Cheng, N. C.; Chen, R. Z.; Mu, S. C.; Sun, X. L. Defects enriched hollow porous Co-N-doped carbons embedded with ultrafine CoFe/Co nanoparticles as bifunctional oxygen electrocatalyst for rechargeable flexible solid zinc–air batteries. *Nano Res.*, in press, DOI: 10.1007/s12274-020-3127-8.

[28] Ma, T. Y.; Dai, S.; Jaroniec, M.; Qiao, S. Z. Metal-organic framework derived hybrid Co$_3$O$_4$-carbon porous nanowire arrays as reversible oxygen evolution electrodes. *J. Am. Chem. Soc.* **2014**, *136*, 13925–13931.

[29] Xu, L.; Jiang, Q. Q.; Xiao, Z. H.; Li, X. Y.; Huo, J.; Wang, S. Y.; Dai, L. M. Plasma-engraved Co$_3$O$_4$ nanosheets with oxygen vacancies and high surface area for the oxygen evolution reaction. *Angew. Chem., Int. Ed.* **2016**, *55*, 5277–5281.

[30] Wang, Z. C.; Xu, W. J.; Chen, X. K.; Peng, Y. H.; Song, Y. Y.; Lv, C. X.; Liu, H. L.; Sun, J. W.; Yuan, D.; Li, X. Y. et al. Defect-rich nitrogen doped Co$_3$O$_4$/C porous nanocubes enable high-efficiency bifunctional oxygen electrocatalysis. *Adv. Funct. Mater.* **2019**, *29*, 1902875.

[31] Cho, S. A.; Jang, Y. J.; Lim, H. D.; Lee, J. E.; Jang, Y. H.; Nguyen, T. T. H.; Mota, F. M.; Fenning, D. P.; Kang, K.; Shao-Horn, Y. et al. Hierarchical porous carbonized Co$_3$O$_4$ inverse opals via combined block copolymer and colloid templating as bifunctional electrocatalysts in Li-O$_2$ battery. *Adv. Energy Mater.* **2017**, *7*, 1700391.

[32] Lee, K. J.; Shin, D. Y.; Byeon, A.; Lim, A.; Jo, Y. S.; Begley, A.; Lim, D. H.; Sung, Y. E.; Park, H. S.; Chae, K. H. et al. Hierarchical cobalt-nitride and -oxide co-doped porous carbon nanostructures for highly efficient and durable bifunctional oxygen reaction electrocatalysts. *Nanoscale* **2017**, *9*, 15846–15855.

[33] Zhu, Y.; Zhang, Z. Y.; Li, W. Q.; Lei, Z.; Cheng, N. C.; Tan, Y. Y.; Mu, S. C.; Sun, X. L. Highly exposed active sites of defect-enriched derived MOFs for enhanced oxygen reduction reaction. *ACS Sustainable Chem. Eng.* **2019**, *7*, 17855–17862.

[34] Jiang, H.; Liu, Y.; Li, W. Z.; Li, J. Co nanoparticles confined in 3D nitrogen-doped porous carbon foams as bifunctional electrocatalysts for long-life rechargeable Zn–air batteries. *Small* **2018**, *14*, 1703739.

[35] Xia, W.; Zou, R. Q.; An, L.; Xia, D. G.; Guo, S. J. A metal–organic framework route to *in situ* encapsulation of Co@Co$_3$O$_4$@C core@bishell nanoparticles into a highly ordered porous carbon matrix for oxygen reduction. *Energy Environ. Sci.* **2015**, *8*, 568–576.

[36] Aijaz, A.; Masa, J.; Rosler, C.; Xia, W.; Weide, P.; Botz, A. J. R.; Fischer, R. A.; Schuhmann, W.; Muhler, M. Co@Co$_3$O$_4$ encapsulated in carbon nanotube-grafted nitrogen-doped carbon polyhedra as an advanced bifunctional oxygen electrode. *Angew. Chem., Int. Ed.* **2016**, *55*, 4087–4091.

[37] Jiang, Y.; Deng, Y. P.; Fu, J.; Lee, D. U.; Liang, R. L.; Cano, Z. P.; Liu, Y. S.; Bai, Z. Y.; Hwang, S.; Yang, L. et al. Interpenetrating triphase cobalt-based nanocomposites as efficient bifunctional oxygen electrocatalysts for long-lasting rechargeable Zn–air batteries. *Adv. Energy Mater.* **2018**, *8*, 1702900.

[38] Guo, Z. Y.; Wang, F. M.; Xia, Y.; Li, J. L.; Tamirat, A. G.; Liu, Y. R.; Wang, L.; Wang, Y. G.; Xia, Y. Y. *In situ* encapsulation of core–shell-structured Co@Co$_3$O$_4$ into nitrogen-doped carbon polyhedra as a bifunctional catalyst for rechargeable Zn–air batteries. *J. Mater. Chem. A* **2018**, *6*, 1443–1453.

[39] Zhou, Q. Y.; Zhang, Z.; Cai, J. J.; Liu, B.; Zhang, Y. L.; Gong, X. F.; Sui, X. L.; Yu, A. P.; Zhao, L.; Wang, Z. B. et al. Template-guided synthesis of Co nanoparticles embedded in hollow nitrogen doped carbon tubes as a highly efficient catalyst for rechargeable Zn–air batteries. *Nano Energy* **2020**, *71*, 104592.

[40] Fu, J.; Hassan, F. M.; Zhong, C.; Lu, J.; Liu, H.; Yu, A. P.; Chen, Z. W. Defect engineering of chalcogen-tailored oxygen electrocatalysts for rechargeable quasi-solid-state zinc–air batteries. *Adv. Mater.* **2017**, *29*, 1702526.

[41] Pachfule, P.; Shinde, D.; Majumder, M.; Xu, Q. Fabrication of carbon nanorods and graphene nanoribbons from a metal-organic framework. *Nat. Chem.* **2016**, *8*, 718–724.

[42] Guo, J. X.; Ghen, B. L.; Hao, Q.; Nie, J.; Ma, G. P. Pod-like structured Co/CoO$_x$ nitrogen-doped carbon fibers as efficient oxygen reduction reaction electrocatalysts for Zn–air battery. *Appl. Surf. Sci.* **2018**, *456*, 959–966.

[43] Ding, D. N.; Shen, K.; Chen, X. D.; Chen, H. R.; Chen, J. Y.; Fan, T.; Wu, R. F.; Li, Y. W. Multi-level architecture optimization of MOF-templated Co-based nanoparticles embedded in hollow N-doped carbon polyhedra for efficient OER and ORR. *ACS Catal.* **2018**, *8*, 7879–7888.

[44] Zhang, J.; Zheng, C. Y.; Zhang, M. L.; Qiu, Y. J.; Xu, Q.; Cheong, W. C.; Chen, W. X.; Zheng, L. R.; Gu, L.; Hu, Z. P. et al. Controlling N-doping type in carbon to boost single-atom site Cu catalyzed transfer hydrogenation of quinoline. *Nano Res.* **2020**, *13*, 3082–3087.

[45] Guo, Y. Y.; Yuan, P. F.; Zhang, J. N.; Hu, Y. F.; Amiinu, I. S.; Wang, X.; Zhou, J. G.; Xia, H. C.; Song, Z. B.; Xu, Q. et al. Carbon nanosheets containing discrete Co-N$_x$-B$_y$-C active sites for efficient oxygen electrocatalysis and rechargeable Zn–air batteries. *ACS Nano* **2018**, *12*, 1894–1901.

[46] Yu, P.; Wang, L.; Sun, F. F.; Xie, Y.; Liu, X.; Ma, J. Y.; Wang, X. W.; Tian, C. G.; Li, J. H.; Fu, H. G. Co nanoislands rooted on Co-N-C nanosheets as efficient oxygen electrocatalyst for Zn–air batteries. *Adv. Mater.* **2019**, *31*, 1901666.

[47] Guo, D. H.; Shibuya, R.; Akiba, C.; Saji, S.; Kondo, T.; Nakamura, J. Active sites of nitrogen-doped carbon materials for oxygen reduction reaction clarified using model catalysts. *Science* **2016**, *351*, 361–365.

[48] Cheng, Q. Q.; Han, S. B.; Mao, K.; Chen, C.; Yang, L. J.; Zou, Z. Q.; Gu, M.; Hu, Z.; Yang, H. Co nanoparticle embedded in atomically-dispersed Co-N-C nanofibers for oxygen reduction with high activity and remarkable durability. *Nano Energy* **2018**, *52*, 485–493.

[49] Zhu, C. Z.; Shi, Q. R.; Xu, B. Z.; Fu, S. F.; Wan, G.; Yang, C.; Yao, S. Y.; Song, J. H.; Zhou, H.; Du, D. et al. Hierarchically porous M-N-C (M = Co and Fe) single-atom electrocatalysts with robust MN$_x$ active moieties enable enhanced ORR performance. *Adv. Energy Mater.* **2018**, *8*, 1801956.

[50] Jiang, H.; Gu, J. X.; Zheng, X. S.; Liu, M.; Qiu, X. Q.; Wang, L. B.; Li, W. Z.; Chen, Z. F.; Ji, X. B.; Li, J. Defect-rich and ultrathin N doped carbon nanosheets as advanced trifunctional metal-free electrocatalysts for the ORR, OER and HER. *Energy Environ. Sci.* **2019**, *12*, 322–333.

[51] Zhang, M. D.; Dai, Q. B.; Zheng, H. G.; Chen, M. D.; Dai, L. M. Novel MOF-derived Co@N-C bifunctional catalysts for highly efficient Zn–air batteries and water splitting. *Adv. Mater.* **2018**, *30*, 1705431.

[52] Wang, Y. Q.; Yu, B. Y.; Liu, K.; Yang, X. T.; Liu, M.; Chan, T. S.; Qiu, X. Q.; Li, J.; Li, W. Z. Co single-atoms on ultrathin N-doped porous carbon via a biomass complexation strategy for high performance metal–air batteries. *J. Mater. Chem. A* **2020**, *8*, 2131–2139.

[53] Li, X. Y.; Rong, H. P.; Zhang, J. T.; Wang, D. S.; Li, Y. D. Modulating the local coordination environment of single-atom catalysts for enhanced catalytic performance. *Nano Res.* **2020**, *13*, 1842–1855.

[54] Yang, J. R.; Li, W. H.; Wang, D. S.; Li, Y. D. Single-atom materials: Small structures determine macroproperties. *Small Struct.*, in press, DOI: 10.1002/sstr.202000051.

[55] Wang, T. T.; Kou, Z. K.; Mu, S. C.; Liu, J. P.; He, D. P.; Amiinu, I. S.; Meng, W.; Zhou, K.; Luo, Z. X.; Chaemchuen, S. et al. 2D dual-metal zeolitic-imidazolate-framework-(ZIF)-derived bifunctional air electrodes with ultrahigh electrochemical properties for rechargeable zinc-air batteries. *Adv. Funct. Mater.* **2018**, *28*, 1705048.

[56] Wu, J. B.; Zhou, H.; Li, Q.; Chen, M.; Wan, J.; Zhang, N.; Xiong, L. K.; Li, S.; Xia, B. Y.; Feng, G. et al. Densely populated isolated single Co-N site for efficient oxygen electrocatalysis. *Adv. Energy Mater.* **2019**, *9*, 1900149.

[57] Zhang, X. L.; Yang, Z. X.; Lu, Z. S.; Wang, W. C. Bifunctional CoN$_x$ embedded graphene electrocatalysts for OER and ORR: A theoretical evaluation. *Carbon* **2018**, *130*, 112–119.

[58] Wang, H.; Kou, R. H.; Jin, Q.; Liu, Y. Z.; Yin, F. X.; Sun, C. J.; Wang, L.; Ma, Z. Y.; Ren, Y.; Liu, N. et al. Boosting the oxygen reduction performance via tuning the synergy between metal core and oxide shell of metal–organic frameworks–derived Co@CoO$_x$. *ChemElectroChem* **2020**, *7*, 1590–1597.

[59] Zhou, Y.; Sun, S. N.; Song, J. J.; Xi, S. B.; Chen, B.; Du, Y. H.; Fisher, A. C.; Cheng, F. Y.; Wang, X.; Zhang, H. et al. Enlarged Co-O covalency in octahedral sites leading to highly efficient spinel oxides for oxygen evolution reaction. *Adv. Mater.* **2018**, *30*, 1802912.

[60] Qin, J. Y.; Liu, Z. W.; Wu, D. Y.; Yang, J. Optimizing the electronic structure of cobalt via synergized oxygen vacancy and Co-N-C to boost reversible oxygen electrocatalysis for rechargeable Zn-air batteries. *Appl. Catal. B Environ.* **2020**, *278*, 119300.

[61] Peng, Y.; Chen, S. W. Electrocatalysts based on metal@carbon core@shell nanocomposites: An overview. *Green Energy Environ.* **2018**, *3*, 335–351.

[62] Huang, Z. F.; Song, J. J.; Du, Y. H.; Xi, S. B.; Dou, S.; Nsanzimana, J. M. V.; Wang, C.; Xu, Z. J.; Wang, X. Chemical and structural

origin of lattice oxygen oxidation in Co–Zn oxyhydroxide oxygen evolution electrocatalysts. *Nat. Energy* **2019**, *4*, 329–338.

[63] Nørskov, J. K.; Bligaard, T.; Rossmeisl, J.; Christensen, C. H. Towards the computational design of solid catalysts. *Nat. Chem.* **2009**, *1*, 37–46.

[64] Nørskov, J. K.; Abild-Pedersen, F.; Studt, F.; Bligaard, T. Density functional theory in surface chemistry and catalysis. *Proc. Natl. Acad. Sci. USA* **2011**, *108*, 937–943.

[65] Ling, T.; Yan, D. Y.; Jiao, Y.; Wang, H.; Zheng, Y.; Zheng, X. L.; Mao, J.; Du, X. W.; Hu, Z. P.; Jaroniec, M. et al. Engineering surface atomic structure of single-crystal cobalt (II) oxide nanorods for superior electrocatalysis. *Nat. Commun.* **2016**, *7*, 12876.

[66] Nørskov, J. K.; Rossmeisl, J.; Logadottir, A.; Lindqvist, L.; Kitchin, J. R.; Bligaard, T.; Jónsson, H. Origin of the overpotential for oxygen reduction at a fuel-cell cathode. *J. Phys. Chem. B* **2004**, *108*, 17886–17892.

[67] Seh, Z. W.; Kibsgaard, J.; Dickens, C. F.; Chorkendorff, I.; Nørskov, J. K.; Jaramillo, T. F. Combining theory and experiment in electrocatalysis: Insights into materials design. *Science* **2017**, *355*, eaad4998.